



OPEN ACCESS

EDITED BY

Hyang-Sook Hoe,
Korea Brain Research Institute,
South Korea

REVIEWED BY

Giovanni La Penna,
National Research Council (CNR), Italy
Davit Potoyan,
Iowa State University, United States

*CORRESPONDENCE

Jack P. Connor
bsjpc@leeds.ac.uk
Charley Schaefer
charley.schaefer@york.ac.uk

SPECIALTY SECTION

This article was submitted to
Molecular Signalling and Pathways,
a section of the journal
Frontiers in Molecular Neuroscience

RECEIVED 06 June 2022

ACCEPTED 14 September 2022

PUBLISHED 13 October 2022

CITATION

Connor JP, Quinn SD and Schaefer C
(2022) Sticker-and-spacer model for
amyloid beta condensation and
fibrillation.
Front. Mol. Neurosci. 15:962526.
doi: 10.3389/fnmol.2022.962526

COPYRIGHT

© 2022 Connor, Quinn and Schaefer.
This is an open-access article
distributed under the terms of the
[Creative Commons Attribution License
\(CC BY\)](https://creativecommons.org/licenses/by/4.0/). The use, distribution or
reproduction in other forums is
permitted, provided the original
author(s) and the copyright owner(s)
are credited and that the original
publication in this journal is cited, in
accordance with accepted academic
practice. No use, distribution or
reproduction is permitted which does
not comply with these terms.

Sticker-and-spacer model for amyloid beta condensation and fibrillation

Jack P. Connor^{1,2,3*}, Steven D. Quinn^{2,4} and Charley Schaefer^{2*}

¹Department of Biology, University of York, York, United Kingdom, ²School of Physics, Engineering and Technology, University of York, York, United Kingdom, ³Astbury Centre for Structural Molecular Biology, School of Molecular and Cellular Biology, University of Leeds, Leeds, United Kingdom, ⁴York Biomedical Research Institute, University of York, York, United Kingdom

A major pathogenic hallmark of Alzheimer's disease is the presence of neurotoxic plaques composed of amyloid beta ($A\beta$) peptides in patients' brains. The pathway of plaque formation remains elusive, though some clues appear to lie in the dominant presence of $A\beta_{1-42}$ in these plaques despite $A\beta_{1-40}$ making up approximately 90% of the $A\beta$ pool. We hypothesize that this asymmetry is driven by the hydrophobicity of the two extra amino acids that are incorporated in $A\beta_{1-42}$. To investigate this hypothesis at the level of single molecules, we have developed a molecular "sticker-and-spacer lattice model" of unfolded $A\beta$. The model protein has a single sticker that may reversibly dimerise and elongate into semi-flexible linear chains. The growth is hampered by excluded-volume interactions that are encoded by the hydrophilic spacers but are rendered cooperative by the attractive interactions of hydrophobic spacers. For sufficiently strong hydrophobicity, the chains undergo liquid-liquid phase-separation (LLPS) into condensates that facilitate the nucleation of fibers. We find that a small fraction of $A\beta_{1-40}$ in a mixture of $A\beta_{1-40}$ and $A\beta_{1-42}$ shifts the critical concentration for LLPS to lower values. This study provides theoretical support for the hypothesis that LLPS condensates act as a precursor for aggregation and provides an explanation for the $A\beta_{1-42}$ -enrichment of aggregates in terms of hydrophobic interactions.

KEYWORDS

Alzheimer's disease, amyloid, aggregation, condensates, liquid-liquid phase separation, single-molecule, bond-fluctuation model

1. Introduction

Alzheimer's disease (AD), the most common cause of dementia (60–80% of cases [Abeyasinghe et al., 2020](#)), and is a fatal neurodegenerative disease causing severe and devastating cognitive impairment. Age is the biggest risk factor for AD, of which, most cases are sporadic (around 95%) and occur over the age of 65 ([Abeyasinghe et al., 2020](#); [Zhang et al., 2020](#); [Zhao et al., 2020](#); [Ayodele et al., 2021](#)). The exact cause of AD is not fully understood and with better living conditions meaning average life expectancy in developed countries is increasing, the number of cases and the burden of neurodegenerative disease is increasing worldwide. As of 2018, an estimated 50 million people worldwide suffer from dementia, with this number expected to triple by 2050 ([Patterson, 2018](#)).

A major pathogenic hallmark in AD brains is the presence of extracellular neurotoxic plaques made up of amyloid beta ($A\beta$) (Stelzmann et al., 1995; Breijyeh and Karaman, 2020). $A\beta$ is produced from amyloid precursor protein (APP) which is cleaved by α , β and γ secretases (Chen et al., 2017; Guo et al., 2020; Hampel et al., 2021). APP proteolytic cleavage can be separated into non-amyloidogenic and amyloidogenic pathways. We will focus on the amyloidogenic pathway as it is relevant to AD. First APP is cleaved by β secretase into soluble APP β and a 99 amino acid C-terminal fragment (C99). C99 is then cleaved by γ secretase at multiple sites giving rise to $A\beta$ of multiple lengths ranging from 39–51 amino acids (Zhang et al., 2011; Haass et al., 2012). After cleavage, $A\beta$ is secreted from the cell where it can then form oligomers, fibrils, and finally plaques. The amyloid cascade hypothesis suggests that the deposition of $A\beta$ into senile plaques is critical for AD pathology (Hardy and Higgins, 1992; Karran et al., 2011; Castellani et al., 2019) but the exact mechanism and change in AD brains that lead to this neurotoxic aggregation is not fully understood. Recently, this hypothesis has been called into question based on amounting evidence in disagreement. Amyloid deposition does not correlate with neuronal loss (Kametani and Hasegawa, 2018) and amyloid burden can be identified in cognitively unimpaired individuals (Arenaza-Urquijo and Vemuri, 2018; Dubois et al., 2021). Furthermore, clinical trials using therapeutics that target $A\beta$ for degradation have been ineffective thus far (Ricciarelli and Fedele, 2017). A particular issue for anti- $A\beta$ therapeutics is that most treatments focus on clearing insoluble aggregates (Tolar et al., 2019) with increasing evidence suggesting that pre-fibrillar soluble oligomers are orders of magnitude more toxic than fibrils and plaques (Chafekar et al., 2008; Ono et al., 2009; Sengupta et al., 2016; Huang and Liu, 2020). Unlike plaques, oligomers have been shown to impair both synaptic function and structure (Selkoe and Hardy, 2016; Kametani and Hasegawa, 2018). A recent study by Ghadami et al. (2020) has demonstrated that transthyretin is neuroprotective which is achieved by binding to $A\beta$ oligomers, inhibiting primary and secondary nucleation without altering elongation, emphasising the role of oligomers in $A\beta$ -mediated neurotoxicity. Consequently, understanding the role of pre-fibrillar $A\beta$ species such as soluble oligomers and their contribution to AD pathology have gained significant interest in recent years.

The most predominant $A\beta$ species is 40 amino acids long ($A\beta_{1-40}$) and makes up $\sim 90\%$ of the $A\beta$ pool. A less prevalent 42 amino acid long species of $A\beta$ ($A\beta_{1-42}$), which accounts for $\sim 10\%$ of the $A\beta$ population is of particular importance to AD due to a higher aggregation propensity. Compared to $A\beta_{1-40}$, $A\beta_{1-42}$ has a longer chain length that increases a repulsive excluded-volume interaction but adds an attractive hydrophobic interaction due to the addition of two C-terminal hydrophobic amino acids. As such, $A\beta_{1-42}$ has increased aggregation propensity and is a predominant component of senile plaques (Iwatsubo et al., 1994; Tamaoka et al., 1994; Gu

and Guo, 2021). Familial AD mutations in APP, PSEN1, and PSEN2, cause increased production of $A\beta$, with abnormally high levels of $A\beta_{1-42}$ relative to $A\beta_{1-40}$ (Scheuner et al., 1996; Hecimovic et al., 2004; Kumar-Singh et al., 2006; Chávez-Gutiérrez and Szaruga, 2020). Recent work shows that the ratio of $A\beta_{1-42}:A\beta_{1-40}$ in plasma and cerebrospinal fluid can be used as a biomarker for AD diagnosis (Baldeiras et al., 2018; Lehmann et al., 2018; Nakamura et al., 2018; Zetterberg, 2019; Doecke et al., 2020; Mahaman et al., 2022; Teunissen et al., 2022) as it correlates with $A\beta$ deposition (Fandos et al., 2017) and cognitive decline (Yaffe et al., 2011; Pérez-Grijalba et al., 2019; Giudici et al., 2020; Lim et al., 2020). This evidence suggests that an increased ratio of $A\beta_{1-42}:A\beta_{1-40}$ may promote the formation of neurotoxic aggregation and the progression of AD.

Hence, in summary, while the physico-chemical properties of $A\beta$ remains subject to debate, these properties appear to correlate with the structural properties of the aggregates. In this study, we focus our attention on the pathway of self-assembly (Michaels et al., 2020), and aim to understand how this pathway is affected by the molecular properties of $A\beta$, such as hydrophobicity and intrinsic disorder. We hypothesize that when $A\beta_{1-42}$ interacts with $A\beta_{1-40}$ sufficient hydrophobicity is added to enhance self-assembly, while the excluded volume interaction is limited. We will model this on a molecular level by describing the intrinsically disordered protein as chains with hydrophilic and hydrophobic segments, as well as ‘sticky’ building blocks that may reversibly self-ensemble into needle-like aggregates.

The aggregation of intrinsically disordered poly-peptides (IDPs) is an important topic in the biological physics of vital intracellular and extracellular processes. In particular, this class of proteins is known to undergo liquid-liquid phase separation (LLPS) to serve biological functionality, such as the (temporary) formation of membraneless organelles (Shin and Brangwynne, 2017; Jin et al., 2021), but also appears responsible to form large droplet-like precursors for the aggregation of the tau protein (Wegmann et al., 2018), which is another hallmark for AD. Large structures (possibly micellar) of approximately 50 $A\beta$ molecules that are speculated to facilitate $A\beta$ aggregation have also been observed (Wegmann et al., 2018). In the present study, we analyse the self-assembly of single peptides to address the current lack of physical models that explain both the formation of large agglomerates and the transition into fibrillar structures in terms of the molecular properties of the IDPs.

We argue that the general mechanism of coupled LLPS and aggregation is an example of physics that emerges from simple concepts such as (non-specific) hydrophobic interactions, excluded volume, and specific interactions. This is a hopeful scenario, as it implies that we may gain relevant molecular insight into this mechanism using strongly coarse-grained molecular models, rather than full atomistic molecular-dynamics simulations that are computationally too demanding to reach the relevant timescales. A commonly

used coarse-graining approach to capture both the polymer physics of the polypeptide and the localized formation of reversible non-covalent bonds is to develop a sticker-and-spacer model. Such models were originally developed for synthetic associating polymers (Leibler et al., 1991), and were later adopted for disordered, multivalent proteins, including natural silk (Schaefer et al., 2020; Schaefer and McLeish, 2022) and scaffolding proteins in biological condensates (Shin and Brangwynne, 2017 and Choi et al., 2019, 2020). Typical simulation approaches solve the Brownian dynamics of the proteins using simulation software packages such as MARTINI or LAMMPS. A major challenge, which is receiving wide attention from the modeling community (Gissinger et al., 2017; Cui et al., 2018; Raffaelli et al., 2020; Schaefer and McLeish, 2022), remains to couple the (continuum-time) conformational dynamics to model the stochastic (instantaneous) association and dissociation of reversible bonds between the molecules. To circumvent the current methodological challenges, in the present study, we will employ the fully stochastic Bond-Fluctuation Model (Carmesin and Kremer, 1988, 1990), which by modeling the molecular dynamics on a 3D lattice successfully describes the (self-avoiding) random walk statistic of flexible and persistent chains (Bates, 2002; Feric et al., 2016; Harmon et al., 2017), LLPS, Reister et al. (2001), Reister and Müller (2003), ring-polymers (Subramanian and Shanbhag, 2009), and cross-linking reactions (Trautenberg et al., 1995). Crucially, as the dynamics are fully stochastic and discrete, they can be addressed using previously developed kinetic Monte Carlo (kMC) schemes (Lukkien et al., 1998).

In the following, we will present a simple sticker-and-spacer model for the dimerisation and (linear) oligomerisation of unfolded $A\beta$, where the cooperativity of growth is determined both by the chain conformation (i.e., intrinsic disorder) and by the binding energies for dimerisation/nucleation, ε_n , and elongation, ε_e , and where hydrophobic interactions are modeled using a short-ranged interaction energy, ε_H . Subsequently, we will present the bond-fluctuation model (BFM) using which we simulate the aggregation of the $A\beta$. In our analysis, we first investigate how the hydrophobic interactions affect the partial collapse of the molecule, and how it may lead to LLPS. We then show that these interactions facilitate dimerisation, as well as the further cooperative growth into longer oligomers. Finally, we demonstrate that increasing $A\beta_{1-42}$ relative to $A\beta_{1-40}$ promotes aggregation.

2. Theory and method

2.1. Introduction: Equilibrium statistics of self-assembly

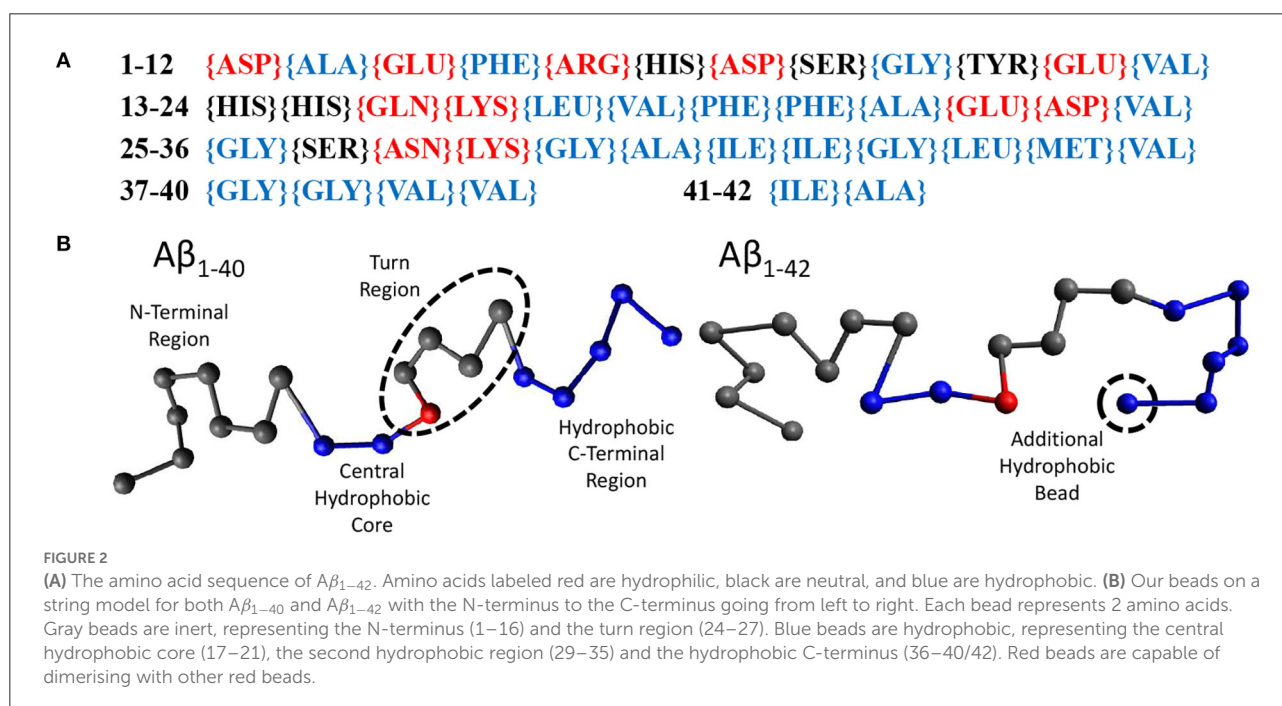
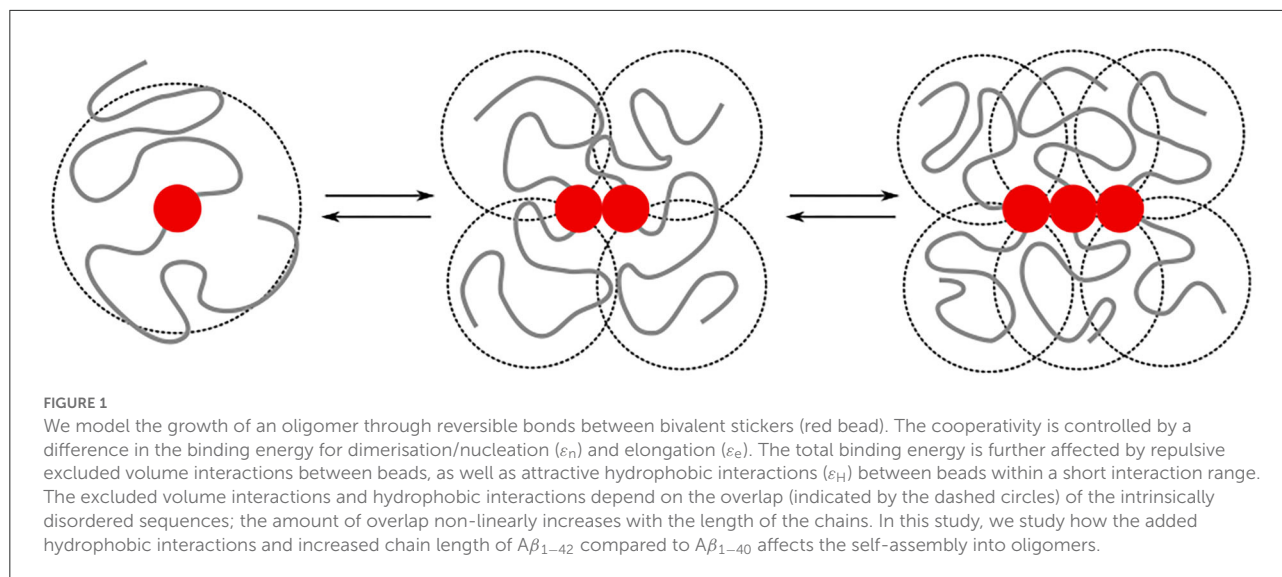
The irreversible formation of $A\beta$ aggregates is nucleated by oligomers, which themselves are reversible and on most

occasions re-dissolve into $A\beta$ monomers (Michaels et al., 2020). The formation of oligomers can on a coarse-grained scale, be described by chemical-reaction equations of the form $A_1 \rightleftharpoons A_n$, where $n > 1$ is the order of the reaction. This reaction order gives a measure for the size of the oligomers but does not provide any structural information [e.g., whether the oligomers are amorphous clusters, rings, or linear chains, and if there are parallel or anti-parallel assemblies of poly-peptide sequences (Miller et al., 2010)]. While this structural information is typically studied at the level of single amino acids and atoms, the observations on the intrinsic disorder in $A\beta$ through its random-coil conformations through both circular dichroism (Danielsson et al., 2005) and nuclear magnetic resonance spectroscopy (Wälti et al., 2015; Roche et al., 2016), begs the question of to what extent concepts from coarse-grained polymer physics can be used to understand the difference in self-assembly behavior of $A\beta_{1-40}$ and $A\beta_{1-42}$. The key idea that we explore is that the specific binding between substrands of the chain leads to interactions between the intrinsically disordered parts of the protein. These include both repulsive excluded-volume interactions and attractive hydrophobic interactions, (Figure 1); their contributions grow non-linearly with the size of the oligomer.

To investigate these ideas, we will describe both species as a randomly coiled polymer that is composed of hydrophilic and hydrophobic beads, as well as one 'sticker' bead. This sticker bead forms reversible intermolecular bonds and leads to the formation of an oligomer. In general, any two oligomers of size $m \geq 1$ and $n \geq 1$ may reversibly assemble into an aggregate of size $m + n$ through the chemical equilibrium equation (Martin, 1996; van der Schoot, 2005; de Greef et al., 2009).



The equilibrium constants of the reactions are non-universal and may be different for each oligomerisation step due to the formation of rings (Cates and Candau, 1990) or due to detailed phenomena, such as the parallel and anti-parallel assembly of poly-peptides. These different mechanisms may be summarised into generic schemes of (anti-)cooperative growth, where in the anti-cooperative case the nucleus is stable and only grows into larger species at high chemical potentials, whereas in the cooperative case, the nucleus is unstable and, once formed, either re-dissolves or rapidly grows into larger (stable) species. As the exact nature of the $A\beta$ species is still under debate, we here represent these overall ideas by a simple 'dimerisation-and-elongation' model (de Greef et al., 2009; Kulkarni et al., 2017), where we have a precise *in silico* control over the cooperativity of growth. We discuss this binding mechanism of the stickers in detail in Section 2.5. First, we will discuss the parametrisation of the protein as a randomly colloid polymer, discuss the Bond-Fluctuation model by which we simulate its equilibrium statistics, and the simple hydrophobicity model.



2.2. Parametrisation of unfolded $A\beta$

Random walk statistics of polymers typically emerge when the contour length is more than 10 times its persistence length and can be modeled using the ‘Bond-Fluctuation Model’ (refer to next Section). The smallest length scale of this model is the persistence length which for polypeptides is one or a few amino acids. Using these considerations, we have chosen to use 20 beads to model $A\beta_{1-40}$ and 21 beads to model $A\beta_{1-42}$. Within our model, a bead may either be hydrophilic, hydrophobic, or may be a sticker. We have parameterised this model using the

sequence of amino acids in $A\beta_{1-42}$, (Figure 2A), which displays the hydrophilic residues in red, the neutral ones in black, and the hydrophobic ones in blue. Our model for $A\beta$ (Figure 2B) was based on the structure of $A\beta_{1-42}$ in Zhu et al. (2012). The first eight gray beads represent the first 16 amino acids corresponding to the hydrophilic N-terminal region. The central hydrophobic core is modeled as two blue (hydrophobic) beads representing amino acids 17–21. A red ‘sticky’ bead which is capable of dimerising with other red beads was added into the turn region to recapitulate the intra- and inter-chain salt bridges that can occur in this region. The remaining hydrophobic beads

represent the C-terminal region with $A\beta_{1-42}$ containing one extra bead to account for the addition of two hydrophobic amino acids. In principle, the properties of the beads may be informed from MD simulations or structural information. However, at this high level of coarse graining the exact sequence is not expected to qualitatively alter the conclusions of our study, in which we have only observed the formation of linear oligomers (i.e., the stickers bind into supramolecular chains) and droplets, but in which no higher-order self-assembled structures such as micelles or membranes were formed (see Results). These may be expected if the hydrophobic/hydrophilic beads would have been arranged into a co-block configuration, and/or if the stickers would have been placed at the chain ends.

2.3. Method: Bond-fluctuation model

We model the chain conformations by placing the polymer segments on the sites of a discrete lattice, following the so-called Bond-Fluctuation Model (BFM) (Carmesin and Kremer, 1988, 1990). This approach originates from the success of lattice models to predict phenomena such as LLPS, including in conditions near the critical point where the correlation-length diverges and mean-field models break down (Hohenberg and Halperin, 1977; Schaefer, 2018; Schaefer et al., 2019). Similarly, the lattice models have provided computationally efficient means to sample the configuration space of polymers. Early lattice models for polymers place polymer segments on a single lattice site (Binder, 1987) but underestimated the Rouse dynamics of the chains due to kinetically trapped states. This was remedied in the BFM by letting a segment occupy 8 sites on a 3D cubic lattice (4 sites on a 2D square lattice) and where the bond lengths can fluctuate from 2 to $\sqrt{10}$ in lattice units (Carmesin and Kremer, 1988, 1990). This approach was proven competitive with off-lattice models both in terms of computational convenience and in physical accuracy in (and beyond) the examples mentioned in the Introduction (Trautenberg et al., 1995; Reister et al., 2001; Bates, 2002; Reister and Müller, 2003; Subramanian and Shanbhag, 2009; Choi et al., 2019).

Within the BFM, the polymer conformations and/or dynamics are modeled using kinetic Monte Carlo (kMC) time steps in which a monomer may move in 6 directions on the lattice if this does not (1) overstretch or understretch the bond between two monomers within the chain or (2) lead to double-occupied lattice sites. This leads to a list of $N_{\text{enabled}} \leq 6N_{\text{monomers}}$ possible processes that may occur during the time step, of which only one (or none) may take place. Which process, i , may take place is selected using the rate,

$$v_i = \begin{cases} v_0, & \text{if } \Delta E_i \leq 0 \\ v_0 \exp(-\Delta E_i/kT), & \text{if } \Delta E_i > 0, \end{cases} \quad (2)$$

where v_0 is an elementary rate (typically of the order $1 - 100 \mu\text{s}^{-1}$) and where ΔE_i is the change in energy. In the algorithm that we use, a process is randomly selected out of the N_{enabled} list of processes. The process is then executed if the system energy is unchanged or decreases $\Delta E_i \leq 0$. However, if the energy would increase, the process is only executed with a probability $p = \exp(-\Delta E_i/kT)$ and rejected otherwise; this decision is carried out using random numbers drawn using a SIMD-oriented Fast Mersenne Twister (Saito and Matsumoto, 2008). Regardless, if the process is accepted or rejected, the time is increased with $\Delta t = 1/(N_{\text{enabled}}v_0)$. The computational efficiency of the method relies on the fact that following a Monte Carlo step during which monomer moves, only the rates of monomers in the vicinity of this monomer need to be recalculated (Lukkien et al., 1998).

2.4. Parametrisation: Hydrophobicity of spacers

To model the attraction between two hydrophobic monomers we follow the approach by Reister et al., and use a square-well potential (Reister et al., 2001).

$$U(r) = \begin{cases} -\varepsilon_H, & \text{for } r \leq \sqrt{10}, \\ 0, & \text{otherwise,} \end{cases} \quad (3)$$

where r is the distance (in units of the lattice spacing) between the two monomers, and where ε_H describes non-specific (e.g., hydrophobic) interactions (Reister et al., 2001). This interaction energy enables the parametrisation of intrinsically disordered poly-peptides through the radius of gyration, and may in principle depend on conditions such the temperature and the ionic strength (Müller-Späth et al., 2010; Wuttke et al., 2014). This parametrisation is done using the Flory exponent ν , which describes the swelling of a polymer through the radius of gyration as $R_g = lN^\nu/\sqrt{6}$, with l the step length between segments. In good solvent conditions, the chain is swollen due to intramolecular self-excluded volume interactions and $\nu = 0.588$. Completely insoluble chains, described with a large value of ε_H , collapse to a compact sphere with $\nu = 1/3$. At θ conditions, the hydrophobic interactions exactly cancel the excluded-volume interactions and the chain obeys random-walk statistics, which are characterized by $\nu = 1/2$. To find the θ -condition, we measure the radius of gyration for chains with various chain length, N , as a function of ε_H (Paul et al., 2005; Steinhauser, 2005). As R_g^2/N is independent of the chain length at the theta condition, the ε_H value at which all curves intersect represents the θ condition. From Figure 3, we find that this occurs at $\varepsilon_H/k_B T \approx 0.27$ for (homopolymer) chains with identical subunits.

As discussed in the previous section, our model for $A\beta$ describes the protein as a copolymer with both hydrophilic

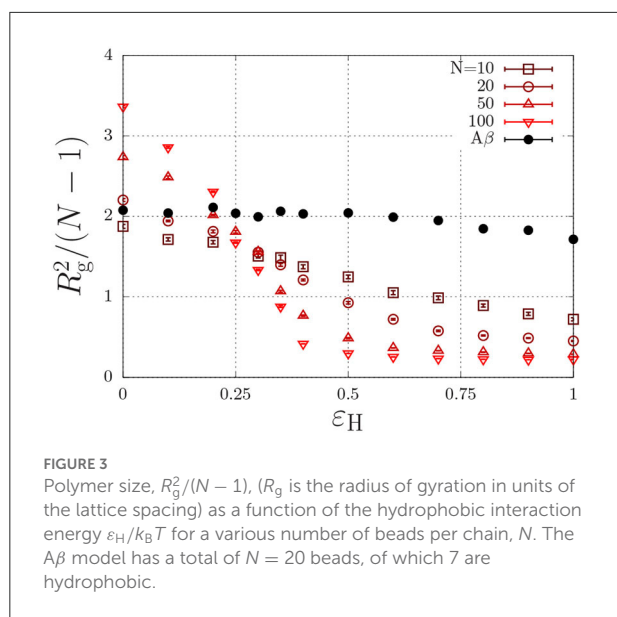


FIGURE 3
 Polymer size, $R_g^2/(N - 1)$, (R_g is the radius of gyration in units of the lattice spacing) as a function of the hydrophobic interaction energy $\epsilon_H/k_B T$ for a various number of beads per chain, N . The $A\beta$ model has a total of $N = 20$ beads, of which 7 are hydrophobic.

and hydrophobic units. The solid circles in Figure 3 show that the radius of gyration, $R_g = lN^\nu/\sqrt{6}$ of this model polypeptide is relatively insensitive to the hydrophobic interaction parameter. To estimate the overlap concentration above which the intramolecular excluded-volume interactions are screened, we use the end-to-end distance, given by $R_e = lN^\nu \approx 3.3$ nm, where $A\beta$ has $N = 40$ amino acids, and where $l = 0.36$ nm is the typical step length of amino acids (Müller-Späh et al., 2010; Wuttke et al., 2014). Using the molecular volume $V_m = (4/3)\pi R_e^3$, we find an overlap concentration of $c_* = M_w/(N_A V_m) \approx 100$ mg/ml = 0.025 M, where we used $M_w = 4.5$ kg/mol. In typical experiments, aggregation is observed well below the overlap concentration (e.g., $A\beta_{1-40}$ aggregates below 1 mg/ml Hortschansky et al., 2005 and $A\beta_{1-42}$ aggregates at concentrations as low as 90 nM Novo et al., 2018).

While those experimental conditions may suggest dilute conditions in which excluded-volume interactions are unimportant, inside LLPS condensates the concentration is significantly higher, and may in fact exceed the overlap concentration. To identify LLPS in our simulations, we focus on structural coarsening phenomena such as Ostwald or Lifshitz-Slyozov-Wagner (LSW) ripening and/or Brownian coalescence (Bray, 2002). The dynamics of coarsening are typically associated with a characteristic length scale (e.g., the radius of a droplet) that grows with the one-third power of time as $R^* - R^0 \propto t^{1/3}$ with R_0 the initial length scale, which may emerge through nucleation or spinodal decomposition. In our simulations, we determine R^* using the following recipe (Singh et al., 2012; Schaefer, 2018; Schaefer et al., 2019): For a given time, t , we calculate the order-parameter field $\psi(\mathbf{r}_i)$, with \mathbf{r}_i the spatial coordinate of a lattice site with i the index of a lattice site. The value of $\psi(\mathbf{r}_i)$ is set to 1 if the site is occupied by a

hydrophobic monomer, and to -1 otherwise. We then calculate the 3D Fourier transform $\hat{\psi}(\mathbf{q})$ and obtain the structure factor $S(q) = \langle |\hat{\psi}(\mathbf{q})|^2 \rangle$, where $\langle \cdot \rangle$ is the spherical/angular average. Next, we obtain the spatial correlation function $C(R)$ as the inverse Fourier transform of $S(q)$. As discussed previously (Singh et al., 2012; Schaefer, 2018; Schaefer et al., 2019), numerically robust measures for the characteristic length scale R^* are the first root (i.e., given by $C(R^*) = 0$) and the first minimum for which $C(R^*) < 0$ and $C'(R^*) = 0$. In our analysis, we will use both measures to assess if structural coarsening occurs in our simulations.

2.5. Parametrisation: Binding of stickers

As motivated in Section 2.1, we will model oligomerisation through the reversible binding of divalent stickers through a ‘dimerisation-and-elongation’ mechanism, where each sticker can either form a single bond or two bonds with other stickers. The dimerisation reaction is



where

$$K_n = \frac{1}{\nu} \exp(-\Delta H_n/k_B T + \Delta S_n/k_B), \tag{5}$$

is the equilibrium constant for nucleation, with ν the characteristic volume, $\Delta H < 0$ is the binding enthalpy and with $\Delta S_n > 0$ the entropic penalty of dimerisation. In this equation, ΔH_n is controlled by the binding energy $\epsilon_n > 0$ and the hydrophobic interaction strength ϵ_H . In the absence of hydrophobic interactions, $\Delta H_n = -\epsilon_n$ is exact. The entropic penalty essentially originates from an excluded-volume interaction due to a limitation of the internal degrees of freedom (DOF) of two chains that undergo dimerisation (refer to Section 3.1). In that section, we will show that these internal DOF are affected by the hydrophobicity (an increased hydrophobicity partially collapses the chain and limits the DOF prior to dimerisation), and by the concentration (above the overlap concentration the free chains have fewer DOF prior to dimerisation), such that an increasing hydrophobicity and concentration reduce the entropic penalty and enhance dimerisation.

For subsequent oligomerisation steps, i.e., for $n > 1$, we describe the equilibrium statistics using



with

$$K_e = \frac{1}{\nu} \exp(-\Delta H_e/k_B T + \Delta S_e/k_B), \tag{7}$$

in which $\Delta H_e/k_B T = -\epsilon_n + U_{\text{hydrophobic}} + U(\theta)$ is composed of an oligomeration/elongation energy, $\epsilon_n > 0$, and hydrophobic

interactions as before. The free energy of binding is modeled as completely entropic using a square-well bending potential (BFM simulations with smoother potentials were previously discussed in the literature, refer to Weber et al., 1999; Bates, 2002; Paul et al., 2005).

$$U(\theta) = \begin{cases} \infty, & \text{for } |\theta - \pi| \leq \theta_{\max}, \\ 0, & \text{otherwise,} \end{cases} \quad (8)$$

for the angle, θ , between the intermolecular bonds between stickers. Here, $\theta = \pi$ represents fully extended bonds. Hence, for small values of θ_{\max} , the persistence length increases and the chain of stickers approaches a rigid rod. In our simulations, we set $\theta_{\max} = \pi/18$ (equivalent to 10 degrees), which ensures sufficient rigidity to avoid ring formation but sufficient flexibility to avoid lattice artifacts.

One of the key predictions of our simulations will be the dependence of the fraction of aggregated material on the concentration and hydrophobicity. We will interpret these findings using analytical predictions in the limit where hydrophobic interactions are absent and where the entropic penalties are constant. In this limit, there exist some known analytical predictions (van der Schoot, 2005). The starting point to obtain these is by writing the equilibrium constants as $K_n = [A_2]/[A_1]^2$ and as $K_e = [A_{n+1}]/[A_n][A_1]$, which are constant for all $n \geq 2$, so that the concentration of any aggregate $[A_n]$ with $n \geq 2$, can be expressed in terms of the concentration of unbound $A\beta$, $[A_1]$, as

$$K_e[A_n] = \sigma(K_e[A_1])^n, \quad (9)$$

with $\sigma \equiv K_n/K_e$ the so-called cooperativity factor.

The concentrations of unbound $A\beta$ is obtained from the mass balance,

$$\begin{aligned} \rho &= \sum_{n=1}^{\infty} n[A_n] \Rightarrow K_e\rho = K_e[A_1] + \sigma \sum_{n=2}^{\infty} n(K_e[A_1])^n \\ &= \sigma \frac{K_e[A_1]}{(1 - K_e[A_1])^2}, \end{aligned} \quad (10)$$

where ρ is the (experimentally-controlled) overall concentration of $A\beta$. Using the standard sum $\sum_{n=1}^{\infty} nx^n = x/(1-x)^2$ for $|x| < 1$ and the fraction of aggregated molecules, $f \equiv 1 - [A_1]/\rho$, this mass balance can be written as Martin (1996) and de Greef et al. (2009).

$$0 = -f + \sigma \frac{K_e\rho[1-f]^2(2 - K_e\rho[1-f])}{(1 - K_e\rho[1-f])^2}, \quad (11)$$

which provides an implicit dependence of f on ρ .

This equation has three asymptotic limits of interest, namely the strongly anti-cooperative case where dimers do not grow into larger aggregates, $K_e \rightarrow 0$ (resulting in $\sigma \rightarrow \infty$) leads to Martin (1996).

$$f = 1 - \frac{-1 + \sqrt{1 + 8K_n\rho}}{4K_n\rho}. \quad (12)$$

In the non-cooperative case, or “isodesmic” case (Smulders et al., 2010), $K \equiv K_e = K_n$ (Martin, 1996),

$$f = 1 - \frac{1 + 2K\rho - \sqrt{1 + 4K\rho}}{2(K\rho)^2}, \quad (13)$$

and in the strongly cooperative case, $\sigma \rightarrow 0$ (van der Schoot, 2005; Smulders et al., 2010), we have $f = 0$ for $K_e\rho < 0$ and

$$f = 1 - \frac{1}{K_e\rho}, \quad (14)$$

for $K_e\rho \geq 0$. These equations show that from the anti-cooperative to the cooperative case, the transition from unbound to aggregated material becomes increasingly sharp. In the following, we will discuss the influence of hydrophobic and excluded-volume interactions on self-assembly in terms of the elongation constant K_e and the cooperativity factor, σ .

3. Results and discussion

3.1. Dimerisation and LLPS

To investigate how hydrophobic and steric interactions affect dimerisation, we have compared the self-assembly of chains with such interactions to the completely hydrophilic counterpart with $\varepsilon_H = 0$, and disabled oligomerisation (i.e., $\varepsilon_e = 0$). We have then simulated the molecular self-assembly of 100 chains in a periodic simulation box with sizes ranging from $50 \times 50 \times 50$ to $1,000 \times 1,000 \times 1,000$, with dimerisation energies ranging from $\varepsilon_n = 2$ to $10k_B T$. The resulting fraction of dimerised chains, f , against the number density ρ (in the number of molecules per box size), is represented by the symbols in Figure 4A.

We have curve fitted each data set with fixed dimerisation energy, ε_e , using the dimerisation model of Equation (12) (solid curves) with the equilibrium constant $K_n = K_{n,0} \exp(\varepsilon_n)$. While $K_{n,0}$ is explicitly independent of ε_n , the curve fits yielded the apparent dependence $\ln K_{n,0} \approx 3.0 - 1.1\varepsilon_n$ (Table 1). This is caused by the fact that the dimerization concentration (characterized by the inflection point of the self-assembly curve) shifts to higher concentrations (above the overlap concentration of $\rho \approx 10^{-4}$, see Section 2.4) for decreasing interaction strengths. Following Flory’s approach to self-avoiding walk statistics, we modify the entropy for excluded-volume interactions using a mean-field description, $\Delta S_n = \Delta S_{n,0} + (\partial \Delta S_n / \partial \rho)\rho$, and write $K_n = K_{n,0} \exp(\varepsilon_n + (\partial[\Delta S_n/k_B]/\partial \rho)\rho)$. Using this modification, we have been able to capture all dimerisation curves in Figure 4A with fixed $K_{00} = 6.85$ and excluded-volume correction $(\partial[\Delta S_n/k_B]/\partial \rho) = 1.3 \cdot 10^3$ (dashed curves). As expected, this correction is insignificant below the overlap concentration, $\rho < 10^{-4}$, but significantly affects the self-assembly curves at higher concentrations.

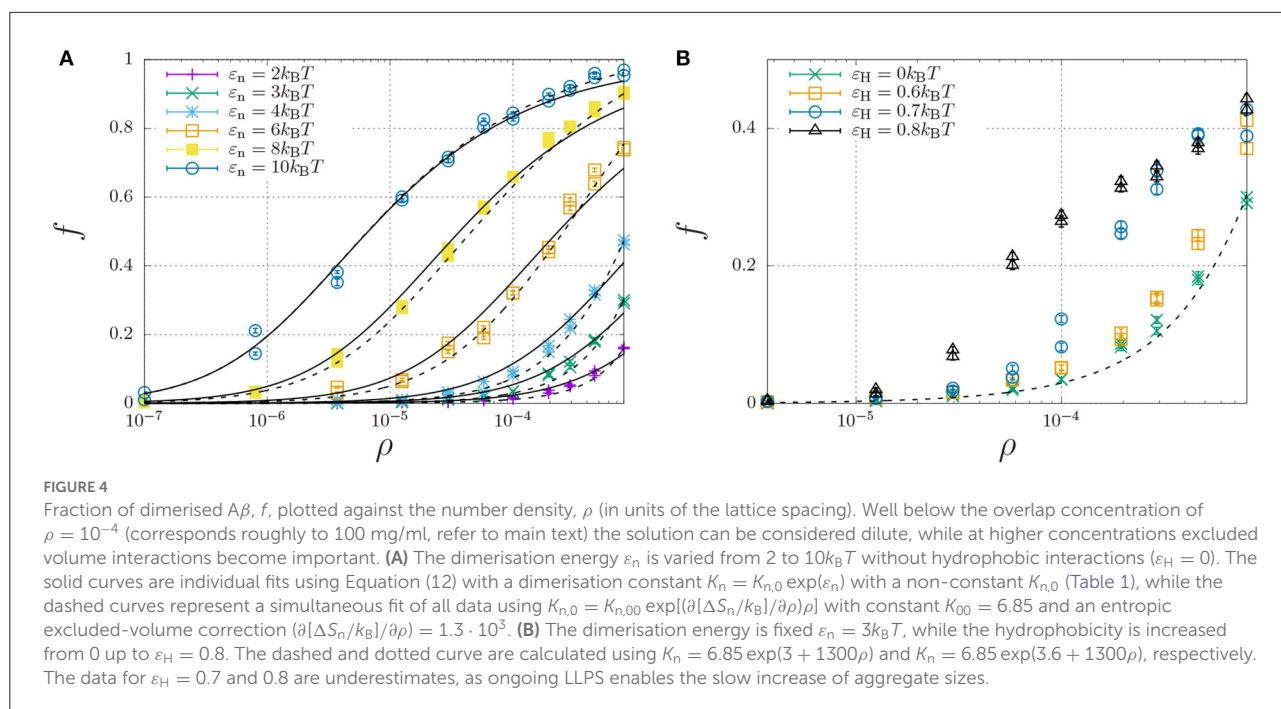


TABLE 1 Values for the equilibrium constant $K_{n,0}$ determined by curve-fitting Equation 12 to the simulated data for various values of the dimerisation energy ϵ_n .

$\epsilon_n/k_B T$	$K_{n,0}$
2	16.63 ± 0.73
3	15.10 ± 0.71
4	13.48 ± 0.82
6	10.61 ± 0.77
8	9.12 ± 0.45
10	6.85 ± 0.37

The curve-fits are shown as solid lines in Figure 4. A lin-log regression yields an apparent relationship $\ln K_{n,0} \approx 3.0 - 1.1\epsilon_n/k_B T$ (refer to main text).

We now focus our attention on the dimerisation curve with $\epsilon_n = 3k_B T$, which has a very low fraction of dimers below the overlap concentration but a finite fraction of dimers at higher concentrations, and increase the hydrophobic-interaction parameter, ϵ_H , from 0 to $0.8k_B T$ (Figure 4B). We find that up to a value of $0.6k_B T$, the hydrophobicity appears to only modestly modify the equilibrium constant as $K_n \approx 6.85 \exp(\epsilon_n + \epsilon_H + 1300\rho)$; we speculate that only the central hydrophobic beads contribute to the enhancement of dimerisation. For stronger hydrophobic interactions, however, the shape of the self-assembly curve can no longer be described using the simple dimerisation model.

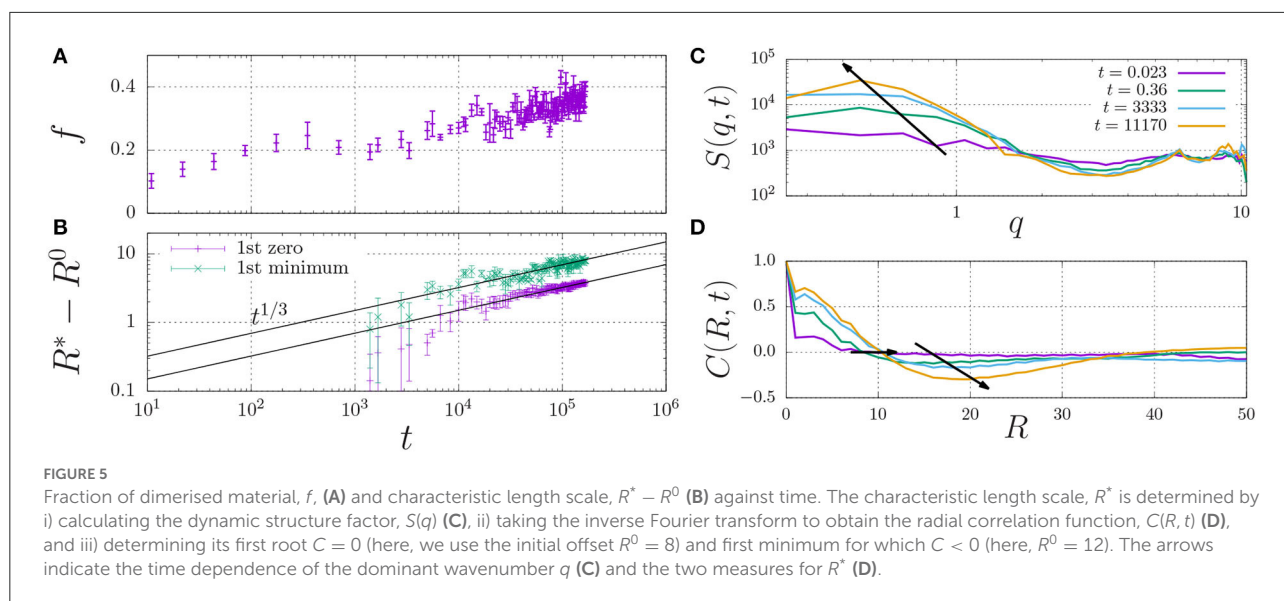
In fact, the datapoint for $\epsilon_H \geq 0.7$ in Figure 4B is not fully converged, and the fraction of dimers increases in a slow process,

as indicated in Figure 5A. This figure shows that the fraction of dimers, f , reaches a plateau at $f \approx 0.2$ for times $t > 100$ up to $t \approx 3,000$, but then slowly increases up to $f \approx 0.4$ at $t = 10^5$ without any sign of convergence to a higher plateau value. This process is a consequence of the slow formation of large structures, as indicated by the typical length scales in the system Figure 5B, which increase as $R^* - R^0 \propto t^{1/3}$, which is a hallmark of LLPS, refer to Section 2.4. Here, we determined R^* using the structure factor $S(q, t)$ (top right), and its corresponding spatial correlation function, $C(R, t)$, (bottom right). We quantified R^* using the first root ($C(R^*, t) = 0, R^0 = 8$) and the first minimum ($C(R_*, t) < 0$ and $\partial C/\partial R = 0, R^0 = 12$).

These findings indicate that sufficiently strong hydrophobic interactions may lead to the formation of droplets through LLPS, which inside the droplets increases the concentration of dimerising units beyond the overlap concentration (which screens the excluded-volume interactions), and provides the mass action needed to induce dimerisation.

3.2. Oligomerisation

Now that we have investigated the dimerisation of $A\beta$, we will investigate the growth of larger oligomers. For that purpose, we again first focus on the case without any hydrophobic interactions, as this enables us to isolate the impact of excluded-volume interactions on the (anti-)cooperativity of self-assembly. This also enables us to select nucleation and elongation energies



of interest in the subsequent simulations, in which we do switch on hydrophobic interactions. Akin to the dimerisation case, we have simulated the self-assembly of 100 $A\beta_{1-40}$ chains in box sizes ranging from $36 \times 36 \times 36$ to $500 \times 500 \times 500$. In these simulations, we have switched off the non-specific/hydrophobic interactions $\varepsilon_H = 0$ and varied the nucleation energies in the range $\varepsilon_n = 1 - 9k_B T$ and the elongation energies in the range $\varepsilon_e = 8 - 14k_B T$.

The simulations yielded the fraction of aggregated material, f , as a function of the concentration, to which we have curve fitted the theoretical model of **Equation (11)**. From the curve-fits, we have extracted the cooperativity factor σ and the equilibrium constant $K_{e,0}$ as a function of the dimerisation energy. Here, $K_{e,0}$ is defined by

$$K_e = v^{-1} \exp(-\Delta H_e + \Delta S_e/k_B) \equiv K_{e,0} \exp(\varepsilon_e/k_B T). \quad (15)$$

The results are tabulated in **Table 2** and plotted in **Figures 6B,C** (discussed below).

A representative self-assembly curve, obtained for fixed $\varepsilon_e = 9k_B T$, is shown in **Figure 6A**. This panel shows the fraction of aggregated material, f , increases with an increasing number density, ρ . The sigmoidal curve becomes increasingly sharp with decreasing dimerisation energy, which, as expected (refer to Section 2.5), indicates increasing cooperativity of self-assembly. Indeed, **Figure 6B** shows that the logarithm of the cooperativity factor increases linearly with increasing dimerisation energy, as expected. On the other hand, the elongation constant $K_{e,0}$ is in principle expected to be independent of the dimerisation energy; however, **Figure 6C** shows it apparently decreases with increasing dimerisation energy. We attribute this apparent dependence to the excluded-volume interactions becoming

more present at higher concentrations, as we found above in the dimerisation curves of **Figure 4**.

To investigate the effect of non-specific hydrophobic interaction on oligomerisation, we have used the parameters $\varepsilon_n = 3k_B T$ and $\varepsilon_e = 9k_B T$ of a hydrophilic chain that cooperatively self-assembles at reasonably high concentrations. This ensured that low-concentration structuring due to hydrophobic interactions would not necessitate larger (and computationally expensive) box sizes. We have then used the sequences for the $A\beta_{1-40}$ and $A\beta_{1-42}$ chains and varied the hydrophobic interaction energy ε_H from 0.4 to $0.7k_B T$. We have again simulated 100 chains in box sizes ranging from $36 \times 36 \times 36$ to $500 \times 500 \times 500$ lattice sites.

We have presented the results in **Figures 7A,B**, displaying the fraction of aggregated material f against the number density ρ for $A\beta_{1-40}$ (**Figure 7A**) and $A\beta_{1-42}$ (**Figure 7B**). In line with our results on dimerisation, we find that increasing hydrophobic interaction energy shifts the aggregation concentration to a lower concentration and that the transition to the aggregates state becomes sharp. For these higher hydrophobicities, we again find a slow ongoing increase of the fraction of aggregated material due to Ostwald ripening and/or rare events of fusion of condensates. After close inspection of **Figures 7A,B**, we observe that the transition occurs for $A\beta_{1-42}$ at lower concentrations than for $A\beta_{1-40}$, which we attribute to a larger number of hydrophobic interactions for the longer chain. Indeed, **Figure 7C** shows that the mean aggregate size at $\rho = 2 \cdot 10^{-4}$ sharply increases at $\varepsilon_H = 0.6$ for the longer chain and at $\varepsilon_H = 0.65$ for the shorter chain. The mean values of the aggregate size are biased by the presence of small oligomers; **Figure 7D** reveals the presence of aggregates with 8 or more chains.

TABLE 2 Shown are the results from varying ε_n for multiple different values of ε_e , in the absence of hydrophobic interactions i.e., $\varepsilon_H = 0k_B T$.

$\varepsilon_n/k_B T$	$\varepsilon_e/k_B T$	σ	$K_{n,0}$
1	8	$2.15 \times 10^{-3} \pm 2.31 \times 10^{-3}$	$2.24 \times 10^{-4} \pm 1.08 \times 10^{-5}$
3	8	$5.41 \times 10^{-2} \pm 1.24 \times 10^{-2}$	$1.82 \times 10^{-4} \pm 8.96 \times 10^{-6}$
5	8	$3.91 \times 10^{-1} \pm 3.73 \times 10^{-2}$	$1.26 \times 10^{-4} \pm 5.83 \times 10^{-6}$
7	8	$1.90 \pm 1.65 \times 10^{-1}$	$7.29 \times 10^{-5} \pm 4.43 \times 10^{-6}$
9	8	8.15 ± 2.10	$3.87 \times 10^{-5} \pm 8.80 \times 10^{-6}$
1	9	$1.33 \times 10^{-4} \pm 4.68 \times 10^{-4}$	$3.87 \times 10^{-4} \pm 1.89 \times 10^{-5}$
3	9	$2.10 \times 10^{-2} \pm 9.29 \times 10^{-3}$	$3.25 \times 10^{-4} \pm 1.72 \times 10^{-5}$
5	9	$2.34 \times 10^{-1} \pm 3.38 \times 10^{-2}$	$2.38 \times 10^{-4} \pm 1.31 \times 10^{-5}$
7	9	$1.50 \pm 1.54 \times 10^{-1}$	$1.61 \times 10^{-4} \pm 1.11 \times 10^{-5}$
9	9	5.55 ± 1.54	$7.92 \times 10^{-5} \pm 1.86 \times 10^{-5}$
1	10	$1.00 \times 10^{-5} \pm 1.54 \times 10^{-4}$	$6.89 \times 10^{-4} \pm 3.19 \times 10^{-5}$
3	10	$5.34 \times 10^{-3} \pm 3.74 \times 10^{-3}$	$5.83 \times 10^{-4} \pm 2.60 \times 10^{-5}$
5	10	$1.53 \times 10^{-1} \pm 3.04 \times 10^{-2}$	$4.49 \times 10^{-4} \pm 2.87 \times 10^{-5}$
7	10	$1.08 \pm 1.36 \times 10^{-1}$	$3.26 \times 10^{-4} \pm 2.55 \times 10^{-5}$
9	10	6.02 ± 1.43	$2.10 \times 10^{-4} \pm 4.26 \times 10^{-5}$
1	11	$1.00 \times 10^{-5} \pm 7.55 \times 10^{-5}$	$1.15 \times 10^{-3} \pm 3.72 \times 10^{-5}$
3	11	$9.06 \times 10^{-3} \pm 5.57 \times 10^{-3}$	$1.05 \times 10^{-3} \pm 5.99 \times 10^{-5}$
5	11	$8.19 \times 10^{-2} \pm 2.17 \times 10^{-2}$	$7.98 \times 10^{-4} \pm 5.03 \times 10^{-5}$
7	11	$8.85 \times 10^{-1} \pm 1.15 \times 10^{-1}$	$6.62 \times 10^{-4} \pm 5.07 \times 10^{-5}$
9	11	4.60 ± 1.18	$4.64 \times 10^{-4} \pm 9.82 \times 10^{-5}$
1	12	$4.58 \times 10^{-5} \pm 1.79 \times 10^{-4}$	$2.23 \times 10^{-3} \pm 7.59 \times 10^{-5}$
3	12	$3.77 \times 10^{-3} \pm 3.18 \times 10^{-3}$	$1.83 \times 10^{-3} \pm 8.20 \times 10^{-5}$
5	12	$8.19 \times 10^{-2} \pm 1.61 \times 10^{-2}$	$1.51 \times 10^{-3} \pm 6.71 \times 10^{-5}$
7	12	$5.94 \times 10^{-1} \pm 9.53 \times 10^{-2}$	$1.19 \times 10^{-3} \pm 9.93 \times 10^{-5}$
9	12	$2.88 \pm 5.63 \times 10^{-1}$	$7.77 \times 10^{-4} \pm 1.15 \times 10^{-4}$
1	14	$5.95 \times 10^{-3} \pm 5.23 \times 10^{-3}$	$8.12 \times 10^{-3} \pm 5.12 \times 10^{-4}$
3	14	$1.65 \times 10^{-2} \pm 1.14 \times 10^{-2}$	$7.99 \times 10^{-3} \pm 6.79 \times 10^{-4}$
5	14	$7.83 \times 10^{-2} \pm 2.53 \times 10^{-2}$	$4.97 \times 10^{-3} \pm 4.04 \times 10^{-4}$
7	14	$3.26 \times 10^{-1} \pm 6.66 \times 10^{-2}$	$3.43 \times 10^{-3} \pm 3.03 \times 10^{-4}$
9	14	$7.21 \times 10^{-1} \pm 1.36 \times 10^{-1}$	$2.00 \times 10^{-3} \pm 2.07 \times 10^{-4}$

Each simulation used 100 $A\beta_{1-40}$ chains in box sizes ranging from $36 \times 36 \times 36$ to $500 \times 500 \times 500$. Each value of σ and $K_{n,0}$ represents the mean and standard error from 3 separate simulations.

3.3. Aggregation of mixed $A\beta_{1-40}$ and $A\beta_{1-42}$

The difference in the critical concentration for condensation of $A\beta_{1-40}$ and $A\beta_{1-42}$, begs the question of to what extent our simple model can capture the reported observation of $A\beta_{1-42}$ -enhanced aggregation in mixtures of $A\beta_{1-40}$ and $A\beta_{1-42}$ (Kumar-Singh et al., 2006; Zetterberg, 2019). To investigate this, we have carried out *in silico* mixing experiments for two different values of hydrophobicity. First, we have chosen $\varepsilon_H = 0.4k_B T$ as it previously appeared to not have led to different aggregation dynamics of $A\beta_{1-42}$ and $A\beta_{1-40}$. Second, we have chosen ε_H

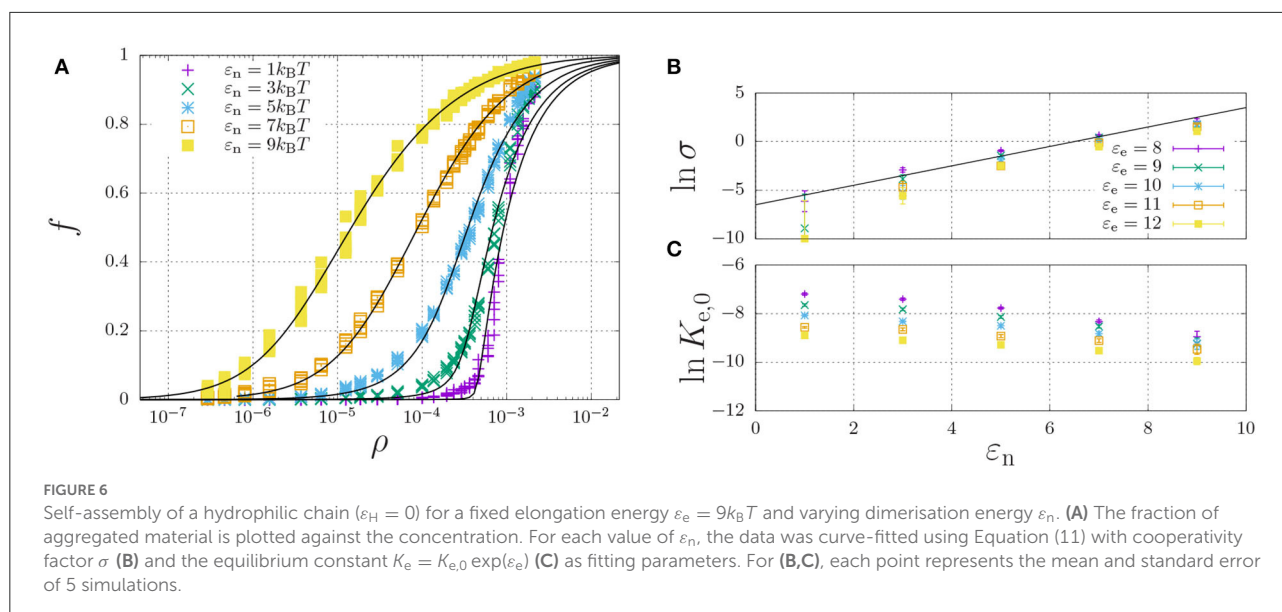
$= 0.6k_B T$, as this value showed the largest difference in the aggregation propensity of the two chains (refer to Figure 7).

In Figure 8, we plot the fraction of aggregated material (Figure 8A) and the mean aggregate size (Figure 8B) against the fraction of $A\beta_{1-42}$ in a mixture of $A\beta_{1-42}$ and $A\beta_{1-40}$. Having in mind that for strong hydrophobicity, structural coarsening renders the system out-of-equilibrium even at long time scales, and thermal equilibrium may never be reached (refer to Figure 5), we have plotted the results after time $4 \cdot 10^6 v_0^{-1}$ and after $4 \cdot 10^7 v_0^{-1}$. As expected, for low hydrophobicity ($\varepsilon_H = 0.4k_B T$), almost no aggregation takes place and the fraction of aggregated materials is ≈ 0.1 , independently of the fraction of long chains. However, for higher hydrophobicity ($\varepsilon_H = 0.6k_B T$) aggregation occurs rapidly for mixtures with 20% $A\beta_{1-42}$ (solid lines), while at long timescale mixtures with 10% $A\beta_{1-42}$ start to aggregate (dotted lines). In qualitative agreement with the experimental observations by Kuperstein et al. (2010), the critical point is strongly biased to a low fraction of $A\beta_{1-42}$ in the mixture ($< 10\%$ in our simulations). The slow dynamics are expected, as it is typical for first-order phase separation near the critical point (Hohenberg and Halperin, 1977). However, we observe another slow process beyond the critical point, namely the increase of the aggregate size at high concentrations of $A\beta_{1-42}$ (panel B). We attribute these to rare events of aggregate fusion.

4. Discussion and conclusion

Our study has contributed a molecular modeling approach to address (1) the observation of $A\beta_{1-42}$ -enhanced toxic plaques associated with Alzheimer's disease, despite being the less concentrated species of $A\beta$, and (2) the hypothesis of condensate-precursors for fibrillation. Here, we sought a molecular explanation for the different self-assembly behavior of $A\beta_{1-40}$ and $A\beta_{1-42}$ using sticker-and-spacer models that capture the intrinsic disorder and the effect of hydrophobicity, while the two extra amino acids in $A\beta_{1-42}$ elongate the chain length, they also add hydrophobicity.

The model predicts a rich range of phenomena due to the interplay between the nucleation and elongation of aggregates with the LLPS of condensates, driven by hydrophobic or other non-specific interactions, which we have summarised in Figure 9. The high concentration inside the condensates enhances the rate of nucleation through the formation of dimers. Furthermore, at these high concentrations the excluded-volume interactions, which in dilute conditions would hamper the growth of aggregates, are screened, such that the cooperativity of oligomerisation is enhanced. Consequently, we find a sharp transition from the unbound to the aggregated state. However, the dynamics by which aggregates may form are slow close to the critical conditions for LLPS. At concentrations above the critical concentration, the growth of aggregates is slow due



to the relatively slow dynamics of Ostwald ripening and/or fusion events.

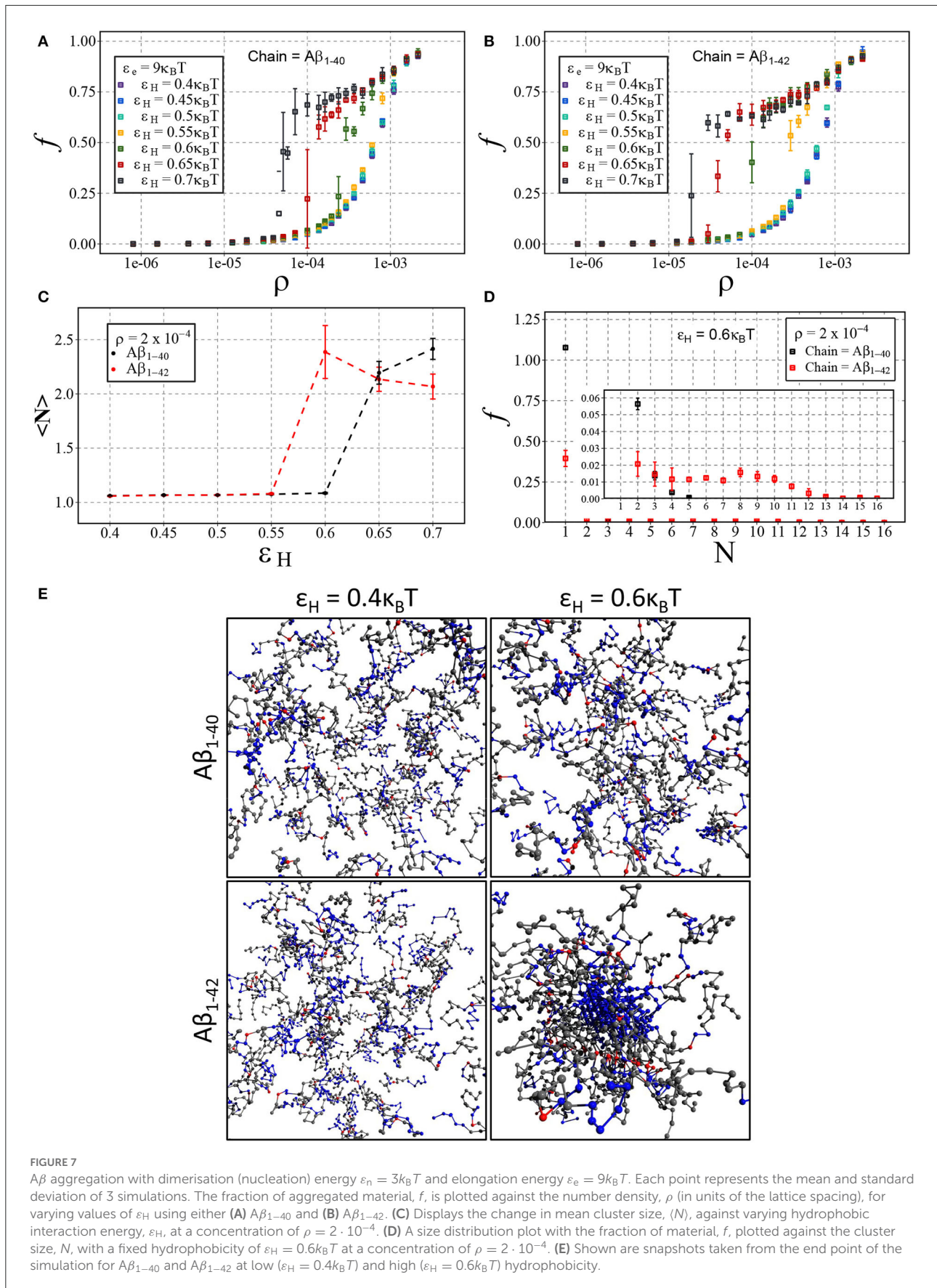
A similar secondary-nucleation mechanism was discussed previously by Cohen et al. (2013) and Michaels et al. (2020), and it was found that the rate constants for primary nucleation, elongation, and secondary nucleation are 100-, 10-, and 3-fold greater, respectively, for $A\beta_{1-42}$ compared to $A\beta_{1-40}$ (Meisl et al., 2014). This provides evidence that the addition of two c-terminal hydrophobic amino acids promotes aggregation propensity, in particular, the rate of primary nucleation. This is in agreement with Roche et al. (2016) who propose that the primary nucleation of $A\beta$ is driven by non-specific hydrophobic interactions which explain the difference in the aggregation rates of $A\beta_{1-40}$ and $A\beta_{1-42}$.

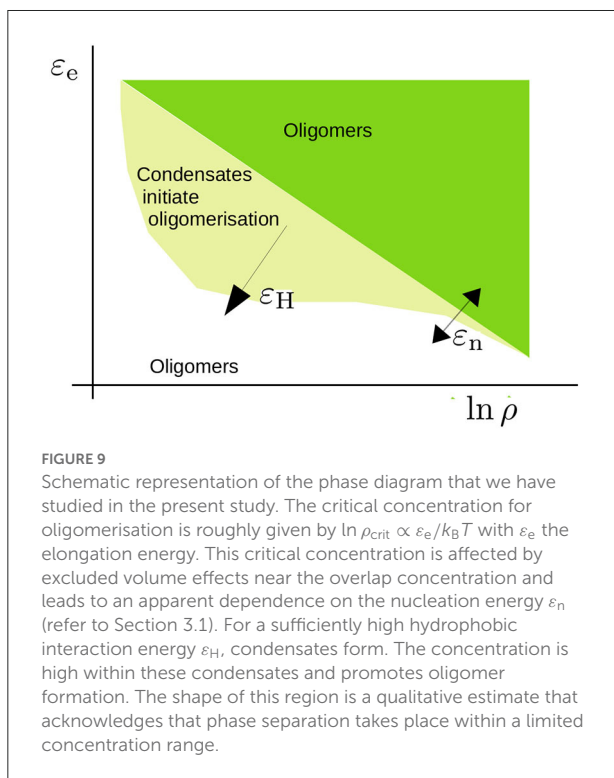
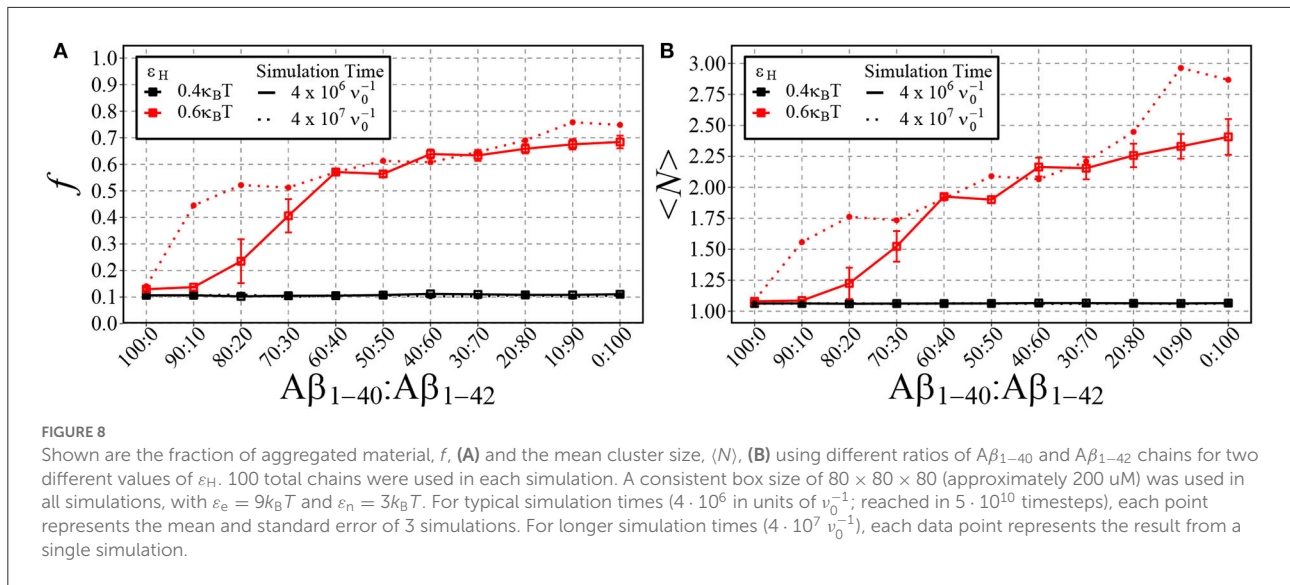
Despite its simplicity, the model also predicts that a small fraction ($< 10\%$) of $A\beta_{1-42}$ in a mixture of $A\beta_{1-42}$ and $A\beta_{1-40}$ shifts the critical concentration for the LLPS of condensates to lower values, which in turn leads to the nucleated self-assembly of fibrillar oligomers at reduced concentrations. This finding is qualitatively consistent with Kuperstein et al. (2010) who found that even a small change from a 1:9 to a 3:7 ratio of $A\beta_{1-42}:A\beta_{1-40}$ caused a dramatic change in the aggregation kinetics and toxicity of the two mixtures *in vitro* and *in vivo*. This 3:7 ratio is of particular importance as it reflects the ratio of $A\beta_{1-42}:A\beta_{1-40}$ observed in familial AD patients (Scheuner et al., 1996) suggesting that maintaining a physiological ratio of $A\beta_{1-42}:A\beta_{1-40}$ is of great importance and may be an effective therapeutic target.

Whether $A\beta_{1-40}$ and $A\beta_{1-42}$ can co-fibrillise is still under debate, Cukalevski et al. (2015) found that mixing $A\beta_{1-40}$ and $A\beta_{1-42}$ leads to the generation of separate

homomolecular fibrils. In contrast, studies have shown that mixing $A\beta_{1-40}$ and $A\beta_{1-42}$ leads to the formation of mixed oligomers and fibrils (Cerofolini et al., 2020; Gu and Guo, 2021). However, it is accepted that $A\beta_{1-40}$ and $A\beta_{1-42}$ interact at the molecular level with increased levels of $A\beta_{1-40}$ inhibiting fibril formation and increased levels of $A\beta_{1-42}$ promoting aggregation (Hasegawa et al., 1999; Yan and Wang, 2007; Jan et al., 2008; Pauwels et al., 2012). Despite studies disagreeing on co-fibrillation, they agree that prefibrillar intermediates consisting of both $A\beta_{1-40}$ and $A\beta_{1-42}$ exist. Our findings suggest that $A\beta_{1-42}$ interacts with $A\beta_{1-40}$, facilitating its aggregation. When only $A\beta_{1-40}$ chains are present and $\epsilon_H = 0.6k_B T$, approximately 10% of the chains are aggregated. However, with $4 \cdot 10^6 v_0^{-1}$, when $A\beta_{1-40}$ and $A\beta_{1-42}$ are mixed at a 60:40 ratio, f increases to approximately 60%. If only $A\beta_{1-42}$ chains are capable of aggregation, $f = 40\%$ at maximum. As this is not the case, it demonstrates that the addition of $A\beta_{1-42}$ is sufficient to promote the aggregation of $A\beta_{1-40}$ under these conditions. One explanation may be that when the more aggregation prone $A\beta_{1-42}$ is present, it forms the primary nuclei overcoming the initial energy barrier that then enables $A\beta_{1-40}$ to aggregate. This theory is supported by Cukalevski et al. (2015) who showed that upon mixing $A\beta_{1-42}$ and $A\beta_{1-40}$ it is $A\beta_{1-42}$ that aggregates first, followed by $A\beta_{1-40}$.

In conclusion, we have presented a simple sticker-and-spacer lattice model that captures a wide range of molecular phenomena of relevance to the literature on $A\beta$ aggregation, which enables us to interpret those phenomena in terms of the simple concepts of nucleation-elongation





models and hydrophobicity and polymeric excluded-volume effects at the level of coarse-grained sticky-polymer models. We hope this approach will lead to further (quantitative) refinements to the understanding of typical experimental time and length scales of $A\beta$ aggregation in few-component *in vitro* and complex multi-component *in vivo* studies.

Data availability statement

The datasets generated/analyzed presented in this study are available on Zenodo <https://doi.org/10.5281/zenodo.7053937>. The simulation code is available on request.

Author contributions

CS and JC collected the data, performed the analysis, and wrote the first draft of the manuscript. CS administered the project and developed, coded the model, and the simulation algorithm. All authors conceived and designed the study, contributed to manuscript revision, read, and approved the submitted version.

Funding

JC acknowledges financial support from the Physics of Life UK. SQ acknowledges support from Alzheimer's Research UK (RF2019-A-001). CS acknowledges support from the Engineering and Physical Sciences Research Council [Grant No. EPSRC (EP/N031431/1)].

Acknowledgments

CS thanks Dr. Ed Higgins, Mitch Aitchison, Thibault Delpech, and Arsenii Zats for their assistance in the development and implementation of the model. CS and JC are grateful for computational support from the University

of York Research and High Performance Computing service, The Viking Cluster.

Conflict of interest

The authors declare that the research was conducted in the absence of any commercial or financial relationships that could be construed as a potential conflict of interest.

References

- Abeyasinghe, A. A. D. T., Deshapriya, R. D. U. S., and Udawatte, C. (2020). Alzheimer's disease: a review of the pathophysiological basis and therapeutic interventions. *Life Sci.* 256, 117996. doi: 10.1016/j.lfs.2020.117996
- Arenaza-Urquijo, E. M., and Vemuri, P. (2018). Resistance vs resilience to Alzheimer disease: clarifying terminology for preclinical studies. *Neurology* 90, 695–703. doi: 10.1212/WNL.0000000000005303
- Ayodele, T., Rogaeva, E., Kurup, J. T., Beecham, G., and Reitz, C. (2021). Early-onset Alzheimer's disease: what is missing in research? *Curr. Neurol. Neurosci. Rep.* 21, 4. doi: 10.1007/s11910-020-01090-y
- Baldeiras, I., Santana, I., Leitão, M. J., Gens, H., Pascoal, R., Tábua-Pereira, M., et al. (2018). Addition of the A β 42/40 ratio to the cerebrospinal fluid biomarker profile increases the predictive value for underlying Alzheimer's disease dementia in mild cognitive impairment. *Alzheimers Res. Therapy* 10, 33. doi: 10.1186/s13195-018-0362-2
- Bates, M. A. (2002). Coarse grained models for flexible liquid crystals: parameterization of the bond fluctuation model. *J. Chem. Phys.* 120, 3986–3997. doi: 10.1063/1.1634551
- Binder, K. (1987). Dynamics of phase separation and critical phenomena in polymer mixtures. *Colloid Polymer Sci.* 265, 273–288. doi: 10.1007/BF01417926
- Bray, A. J. (2002). Theory of phase-ordering kinetics. *Adv. Phys.* 51, 481–587. doi: 10.1080/00018730110117433
- Brijeyeh, Z., and Karaman, R. (2020). Comprehensive review on Alzheimer's disease: causes and treatment. *Molecules* 25, 5789. doi: 10.3390/molecules25245789
- Carmesin, I., and Kremer, K. (1988). The bond fluctuation method: a new effective algorithm for the dynamics of polymers in all spatial dimensions. *Macromolecules* 21, 273–288. doi: 10.1021/ma00187a030
- Carmesin, I., and Kremer, K. (1990). Static and dynamic properties of two-dimensional polymer melts. *J. Phys.* 51, 915–932. doi: 10.1051/jphys:019900051010091500
- Castellani, R. J., Plascencia-Villa, G., and Perry, G. (2019). The amyloid cascade and Alzheimer's disease therapeutics: theory versus observation. *Lab. Invest.* 99, 958–970. doi: 10.1038/s41374-019-0231-z
- Cates, M. E., and Candau, S. J. (1990). Statics and dynamics of worm-like surfactant micelles. *J. Phys.* 2, 6869–6892. doi: 10.1088/0953-8984/2/33/001
- Cerofolini, L., Ravera, E., Bologna, S., Wiglenda, T., Böddrich, A., Purfürst, B., et al. (2020). Mixing A β (1–40) and A β (1–42) peptides generates unique amyloid fibrils. *Chem. Commun.* 56, 8830–8833. doi: 10.1039/D0CC02463E
- Chafekar, S. M., Baas, F., and Scheper, W. (2008). Oligomer-specific A β toxicity in cell models is mediated by selective uptake. *Biochim. Biophys. Acta* 1782, 523–531. doi: 10.1016/j.bbadis.2008.06.003
- Chávez-Gutiérrez, L., and Szaruga, M. (2020). Mechanisms of neurodegeneration-Insights from familial Alzheimer's disease. *Seminars Dev. Biol.* 105, 75–85. doi: 10.1016/j.semdev.2020.03.005
- Chen, G.-f., Xu, T.-h., Yan, Y., Zhou, Y.-r., Jiang, Y., Melcher, K., et al. (2017). Amyloid beta: structure, biology and structure-based therapeutic development. *Acta Pharmacol. Sin.* 38, 1205–1235. doi: 10.1038/aps.2017.28
- Choi, J.-M., Dar, F., and Pappu, R. V. (2019). LASSI: a lattice model for simulating phase transitions of multivalent proteins. *PLoS Comput. Biol.* 15, e611095. doi: 10.1101/611095
- Choi, J.-M., Holehouse, A. S., and Pappu, R. V. (2020). Physical principles underlying the complex biology of intracellular phase transitions. *Annu. Rev. Biophys.* 49, 107–133. doi: 10.1146/annurev-biophys-121219-081629
- Cohen, S. I. A., Linse, S., Luheshi, L. M., Hellstrand, E., White, D. A., Rajah, L., et al. (2013). Proliferation of amyloid- β 42 aggregates occurs through a secondary nucleation mechanism. *Proc. Natl. Acad. Sci. U.S.A.* 110, 9758–9763. doi: 10.1073/pnas.1218402110
- Cui, G., Boudara, V. A. H., Huang, Q., Baeza, G. P., Wilson, A. J., Hassager, O., et al. (2018). Linear shear and nonlinear extensional rheology of unentangled supramolecular side-chain polymers. *J. Rheol.* 62, 1155–1174. doi: 10.1122/1.5012349
- Cukalevski, R., Yang, X., Meisl, G., Weininger, U., Bernfur, K., Frohm, B., et al. (2015). The A β 40 and A β 42 peptides self-assemble into separate homomolecular fibrils in binary mixtures but cross-react during primary nucleation. *Chem. Sci.* 6, 4215–4233. doi: 10.1039/C4SC02517B
- Danielsson, J., Jarvet, J., Damberg, P., and Gräslund, A. (2005). The Alzheimer β -peptide shows temperature-dependent transitions between left-handed 31-helix, β -strand and random coil secondary structures. *FEBS J.* 272, 3938–3949. doi: 10.1111/j.1742-4658.2005.04812.x
- de Greef, T. F. A., Smulders, M. M. J., Wolfs, M., Schenning, A. P. H. J., Sijbesma, R. P., and Meijer, E. W. (2009). Supramolecular polymerization. *Chem. Rev.* 109, 5687–5754. doi: 10.1021/cr900181u
- Doeck, J. D., Pérez-Grijalba, V., Fandos, N., Fowler, C., Villemagne, V. L., Masters, C. L., et al. (2020). Total A β 42/A β 40 ratio in plasma predicts amyloid-PET status, independent of clinical AD diagnosis. *Neurology* 94, e1580–e1591. doi: 10.1212/WNL.0000000000009240
- Dubois, B., Villain, N., Frisoni, G. B., Rabinovici, G. D., Sabbagh, M., Cappa, S., et al. (2021). Clinical diagnosis of Alzheimer's disease: recommendations of the International Working Group. *Lancet Neurol.* 20, 484–496. doi: 10.1016/S1474-4422(21)00066-1
- Fandos, N., Pérez-Grijalba, V., Pesini, P., Olmos, S., Bossa, M., Villemagne, V. L., et al. (2017). Plasma amyloid β 42/40 ratios as biomarkers for amyloid β cerebral deposition in cognitively normal individuals. *Alzheimers Dement.* 8, 179–187. doi: 10.1016/j.dadm.2017.07.004
- Feric, M., Vaidya, N., Harmon, T. S., Mitrea, D. M., Zhu, L., Richardson, T. M., et al. (2016). Coexisting liquid phases underlie nucleolar sub-compartments. *Cell* 165, 1686–1697. doi: 10.1016/j.cell.2016.04.047
- Ghadami, S. A., Chia, S., Ruggeri, F. S., Meisl, G., Bemporad, F., Habchi, J., et al. (2020). Transthyretin inhibits primary and secondary nucleations of Amyloid- β peptide aggregation and reduces the toxicity of its oligomers. *Biomacromolecules* 21, 1112–1125. doi: 10.1021/acs.biomac.9b01475
- Gissinger, J. R., Jensen, B. D., and Wise, K. E. (2017). Modeling chemical reactions in classical molecular dynamics simulations. *Polymer* 128, 211–217. doi: 10.1016/j.polymer.2017.09.038
- Giudici, K. V., de Souto Barreto, P., Guyonnet, S., Li, Y., Bateman, R. J., Vellas, B., and MAPT/DSA Group (2020). Assessment of plasma amyloid- β 42/40 and cognitive decline among community-dwelling older adults. *JAMA Network Open* 3, e2028634. doi: 10.1001/jamanetworkopen.2020.28634
- Gu, L., and Guo, Z. (2021). Alzheimer's A β 42 and A β 40 form mixed oligomers with direct molecular interactions. *Biochem. Biophys. Res. Commun.* 534, 292–296. doi: 10.1016/j.bbrc.2020.11.092

Publisher's note

All claims expressed in this article are solely those of the authors and do not necessarily represent those of their affiliated organizations, or those of the publisher, the editors and the reviewers. Any product that may be evaluated in this article, or claim that may be made by its manufacturer, is not guaranteed or endorsed by the publisher.

- Guo, T., Zhang, D., Zeng, Y., Huang, T. Y., Xu, H., and Zhao, Y. (2020). Molecular and cellular mechanisms underlying the pathogenesis of Alzheimer's disease. *Mol. Neurodegener.* 15, 40. doi: 10.1186/s13024-020-00391-7
- Haass, C., Kaether, C., Thinakaran, G., and Sisodia, S. (2012). Trafficking and proteolytic processing of APP. *Cold Spring Harbor Perspect. Med.* 2, a006270. doi: 10.1101/cshperspect.a006270
- Hampel, H., Hardy, J., Blennow, K., Chen, C., Perry, G., Kim, S. H., et al. (2021). The amyloid- β pathway in Alzheimer's disease. *Mol. Psychiatry* 26, 5481–5503. doi: 10.1038/s41380-021-01249-0
- Hardy, J. A., and Higgins, G. A. (1992). Alzheimer's disease: the amyloid cascade hypothesis. *Science* 256, 184–185. doi: 10.1126/science.1566067
- Harmon, T. S., Holehouse, A. S., Rosen, M. K., and Pappu, R. V. (2017). Intrinsically disordered linkers determine the interplay between phase separation and gelation in multivalent proteins. *Elife* 6, e30294. doi: 10.7554/eLife.30294
- Hasegawa, K., Yamaguchi, I., Omata, S., Gejyo, F., and Naiki, H. (1999). Interaction between A β (1–42) and A β (1–40) in Alzheimer's beta-amyloid fibril formation in vitro. *Biochemistry* 38, 15514–15521. doi: 10.1021/bi991161m
- Hecimovic, S., Wang, J., Dolios, G., Martinez, M., Wang, R., and Goate, A. M. (2004). Mutations in app have independent effects on a β and ctf generation. *Neurobiol. Dis.* 17, 205–218. doi: 10.1016/j.nbd.2004.04.018
- Hohenberg, P. C., and Halperin, B. I. (1977). Theory of dynamic critical phenomena. *Rev. Mod. Phys.* 49, 435–479. doi: 10.1103/RevModPhys.49.435
- Hortschansky, P., Schroeckh, V., Christopeit, T., Zandomenighi, G., and Fändrich, M. (2005). The aggregation kinetics of Alzheimer's β -amyloid peptide is controlled by stochastic nucleation. *Protein Sci.* 14, 1753–1759. doi: 10.1110/ps.041266605
- Huang, Y.-R. and Liu, R.-T. (2020). The toxicity and polymorphism of β -amyloid oligomers. *Int. J. Mol. Sci.* 21, 4477. doi: 10.3390/ijms21124477
- Iwatsubo, T., Odaka, A., Suzuki, N., Mizusawa, H., Nukina, N., and Ihara, Y. (1994). Visualization of A β 42(43) and A β 40 in senile plaques with end-specific A β monoclonals: evidence that an initially deposited species is A β 42(43). *Neuron* 13, 45–53. doi: 10.1016/0896-6273(94)90458-8
- Jan, A., Gokce, O., Luthi-Carter, R., and Lashuel, H. A. (2008). The ratio of monomeric to aggregated forms of A β 40 and A β 42 is an important determinant of amyloid- β aggregation, fibrillogenesis, and toxicity *. *J. Biol. Chem.* 283, 28176–28189. doi: 10.1074/jbc.M803159200
- Jin, X., Li, J.-E., Schaefer, C., Luo, X., Luo, X., Wollman, A. J. M., et al. (2021). Membraneless organelles formed by liquid-liquid phase separation increase bacterial fitness. *Sci. Adv.* 7, eabh2929. doi: 10.1126/sciadv.abh2929
- Kametani, F., and Hasegawa, M. (2018). Reconsideration of amyloid hypothesis and tau hypothesis in Alzheimer's disease. *Front. Neurosci.* 12, 25. doi: 10.3389/fnins.2018.00025
- Karran, E., Mercken, M., and Strooper, B. D. (2011). The amyloid cascade hypothesis for Alzheimer's disease: an appraisal for the development of therapeutics. *Nat. Rev. Drug Discov.* 10, 698–712. doi: 10.1038/nrd3505
- Kulkarni, C., Meijer, E. W., and Palmans, A. R. A. (2017). Cooperativity scale: a structure-mechanism correlation in the self-assembly of benzene-1,3,5-tricarboxamides. *Acc. Chem. Res.* 50, 1928–1936. doi: 10.1021/acs.accounts.7b00176
- Kumar-Singh, S., Theuns, J., Van Broeck, B., Pirici, D., Vennekens, K., Corsmit, E., et al. (2006). Mean age-of-onset of familial Alzheimer disease caused by presenilin mutations correlates with both increased A β 42 and decreased A β 40. *Human Mutation* 27, 686–695. doi: 10.1002/humu.20336
- Kuperstein, I., Broersen, K., Benilova, I., Rozenski, J., Jonckheere, W., Debulpaep, M., et al. (2010). Neurotoxicity of Alzheimer's disease A β peptides is induced by small changes in the A β 42 to A β 40 ratio. *EMBO J.* 29, 3408–3420. doi: 10.1038/emboj.2010.211
- Lehmann, S., Delaby, C., Boursier, G., Catteau, C., Ginestet, N., Tiers, L., et al. (2018). Relevance of A β 42/40 ratio for detection of Alzheimer disease pathology in clinical routine: the PLMR scale. *Front Aging Neurosci.* 10, 138. doi: 10.3389/fnagi.2018.00138
- Leibler, L., Rubinstein, M., and Colby, R. H. (1991). Dynamics of reversible networks. *Macromolecules* 24, 4701–4707. doi: 10.1021/ma00016a034
- Lim, Y. Y., Maruff, P., Kaneko, N., Doecke, J., Fowler, C., Villemagne, V. L., et al. (2020). Plasma Amyloid- β biomarker associated with cognitive decline in preclinical Alzheimer's disease. *J. Alzheimers Dis.* 77, 1057–1065. doi: 10.3233/JAD-200475
- Lukkien, J. J., Segers, J. P. L., Hilbers, P. A. J., Gelten, R. J., and Jansen, A. P. J. (1998). Efficient monte carlo methods for the simulation of catalytic surface reactions. *Phys. Rev. E* 58, 2598–2610. doi: 10.1103/PhysRevE.58.2598
- Mahaman, Y. A. R., Embaye, K. S., Huang, F., Li, L., Zhu, F., Wang, J.-Z., et al. (2022). Biomarkers used in Alzheimer's disease diagnosis, treatment, and prevention. *Ageing Res. Rev.* 74, 101544. doi: 10.1016/j.arr.2021.101544
- Martin, R. B. (1996). Comparisons of indefinite self-association models. *Chem. Rev.* 96, 3044–3064. doi: 10.1021/cr960037v
- Meisl, G., Yang, X., Hellstrand, E., Frohm, B., Kirkegaard, J. B., Cohen, S. I. A., et al. (2014). Differences in nucleation behavior underlie the contrasting aggregation kinetics of the A β 40 and A β 42 peptides. *Proc. Natl. Acad. Sci. U.S.A.* 111, 9384–9389. doi: 10.1073/pnas.1401564111
- Michaels, T. C. T., Saric, A., Curk, S., Bernfur, K., Arosio, P., Meisl, G., et al. (2020). Dynamics of oligomer populations formed during the aggregation of Alzheimer's A β 42 peptide. *Nat. Chem.* 12, 445–451. doi: 10.1038/s41557-020-0452-1
- Miller, Y., Ma, B., and Nussinov, R. (2010). Polymorphism in Alzheimer A β amyloid organization reflects conformational selection in a rugged energy landscape. *Chem. Rev.* 110, 4820–4838. doi: 10.1021/cr900377t
- Müller-Späh, S., Soranno, A., Hirschfeld, V., Hofmann, H., Rügger, S., Reymond, L., et al. (2010). Charge interactions can dominate the dimensions of intrinsically disordered proteins. *Proc. Natl. Acad. Sci. U.S.A.* 107, 14609–14614. doi: 10.1073/pnas.1001743107
- Nakamura, A., Kaneko, N., Villemagne, V. L., Kato, T., Doecke, J., Dore, V., et al. (2018). High performance plasma amyloid- β biomarkers for Alzheimer's disease. *Nature* 554, 249–254. doi: 10.1038/nature25456
- Novo, M., Freire, S., and Al-Soufi, W. (2018). Critical aggregation concentration for the formation of early amyloid- β (1–42) oligomers. *Sci. Rep.* 8, 1783. doi: 10.1038/s41598-018-19961-3
- Ono, K., Condron, M. M., and Teplow, D. B. (2009). Structure-neurotoxicity relationships of amyloid β -protein oligomers. *Proc. Natl. Acad. Sci. U.S.A.* 106, 14745–14750. doi: 10.1073/pnas.0905127106
- Patterson, C. (2018). *World Alzheimer Report 2018. The State of the Art of Dementia Research: New Frontiers. An Analysis of Prevalence, Incidence, Cost and Trends.* Alzheimer's Disease International.
- Paul, W., Muller, M., Binder, K., Stukan, M. R., and Ivanov, V. A. (2005). *Computer Simulations of Liquid Crystals and Polymers: Monte Carlo Simulations of Semi-Flexible Polymers.* Dordrecht: Kluwer Academic Publisher.
- Pauwels, K., Williams, T. L., Morris, K. L., Jonckheere, W., Vandersteen, A., Kelly, G., et al. (2012). Structural basis for increased toxicity of pathological A β 42:A β 40 ratios in Alzheimer disease. *J. Biol. Chem.* 287, 5650–5660. doi: 10.1074/jbc.M111.264473
- Pérez-Grijalba, V., Romero, J., Pesini, P., Sarasa, L., Monleón, I., San-José, I., et al. (2019). Plasma A β 42/40 ratio detects early stages of Alzheimer's disease and correlates with CSF and neuroimaging biomarkers in the AB255 study. *J. Prevent. Alzheimers Dis.* 6, 34–41. doi: 10.14283/jpad.2018.41
- Raffaelli, C., Bose, A., Vrusch, C. H. M. P., Ciarella, S., Davris, T., Tito, N. B., et al. (2020). "Rheology, rupture, reinforcement and reversibility: computational approaches for dynamic network materials," in *Self-Healing and Self-Recovering Hydrogels*, Vol. 285, eds C. Creton and O. Okay (Cham: CRC Press).
- Reister, E., and Müller, M. (2003). Formation of enrichment layers in thin polymer films: the influence of single chain dynamics. *J. Chem. Phys.* 118, 8476–8488. doi: 10.1063/1.1565105
- Reister, E., Müller, M., and Binder, K. (2001). Spinodal decomposition in a binary polymer mixture: dynamic self-consistent-field theory and monte carlo simulations. *Phys. Rev. E* 64, 041804. doi: 10.1103/PhysRevE.64.041804
- Ricciarelli, R., and Fedele, E. (2017). The amyloid cascade hypothesis in Alzheimer's disease: it's time to change our mind. *Curr. Neuropharmacol.* 15, 926–935. doi: 10.2174/1570159X15666170116143743
- Roche, J., Shen, Y., Lee, J. H., Ying, J., and Bax, A. (2016). Monomeric A β 1–40 and A β 1–42 peptides in solution adopt very similar ramachandran map distributions that closely resemble random coil. *Biochemistry* 55, 762–775. doi: 10.1021/acs.biochem.5b01259
- Saito, M., and Matsumoto, M. (2008). "Simd-oriented fast mersenne twister: a 128-bit pseudorandom number generator," in *Monte Carlo and Quasi-Monte Carlo Methods 2006*, eds A. Keller, S. Heinrich and H. Niederreiter (Berlin; Heidelberg: Springer Berlin Heidelberg), 607–622.
- Schaefer, C. (2018). Structuring of fluid adlayers upon ongoing unimolecular adsorption. *Phys. Rev. Lett.* 120, 036001. doi: 10.1103/PhysRevLett.120.036001
- Schaefer, C., Laity, P. R., Holland, C., and McLeish, T. C. B. (2020). Silk protein solution: a natural example of sticky reptation. *Macromolecules* 53, 2669–2676. doi: 10.1021/acs.macromol.9b02630

- Schaefer, C., and McLeish, T. C. B. (2022). Theoretical rheo-physics of silk: Intermolecular associations reduce the critical specific work for flow-induced crystallization. *J. Rheol.* 66, 515–534. doi: 10.1122/8.0000411
- Schaefer, C., Paquay, S., and McLeish, T. C. B. (2019). Morphology formation in binary mixtures upon gradual destabilisation. *Soft Matter*. 15, 8450. doi: 10.1039/C9SM01344J
- Scheuner, D., Eckman, C., Jensen, M., Song, X., Citron, M., Suzuki, N., et al. (1996). Secreted amyloid beta-protein similar to that in the senile plaques of Alzheimer's disease is increased *in vivo* by the presenilin 1 and 2 and APP mutations linked to familial Alzheimer's disease. *Nat. Med.* 2, 864–870. doi: 10.1038/nm0896-864
- Selkoe, D. J., and Hardy, J. (2016). The amyloid hypothesis of Alzheimer's disease at 25 years. *EMBO Mol. Med.* 8, 595–608. doi: 10.15252/emmm.201606210
- Sengupta, U., Nilson, A. N., and Kaye, R. (2016). The role of Amyloid- β oligomers in toxicity, propagation, and immunotherapy. *EBioMedicine* 6, 42–49. doi: 10.1016/j.ebiom.2016.03.035
- Shin, Y., and Brangwynne, C. P. (2017). Liquid phase condensation in cell physiology and disease. *Cell. Biophys.* 357, 1253. doi: 10.1126/science.aaf4382
- Singh, A., Puri, S., and Dasgupta, C. (2012). Growth kinetics of nanoclusters in solution. *J. Phys. Chem. B* 116, 4519. doi: 10.1021/jp211380j
- Smulders, M., Nieuwenhuizen, M., de Greef, T., van der Schoot, P., Schenning, A., and Meijer, E. (2010). How to distinguish isodesmic from cooperative supramolecular polymerisation. *Chem. A Eur. J.* 16, 362–367. doi: 10.1002/chem.200902415
- Steinhauser, M. O. (2005). A molecular dynamics study on universal properties of polymer chains in different solvent qualities. Part I. a review of linear chain properties. *J. Chem. Phys.* 122, 094901. doi: 10.1063/1.1846651
- Stelzmann, R. A., Norman Schnitzlein, H., and Reed Murtagh, F. (1995). An english translation of alzheimer's 1907 paper, "über eine eigenartige erkankung der hirnrinde". *Clin. Anat.* 8, 429–431. doi: 10.1002/ca.980080612
- Subramanian, G., and Shanbhag, S. (2009). Conformational free energy of melts of ring-linear polymer blend. *Phys. Rev. E* 80, 041806. doi: 10.1103/PhysRevE.80.041806
- Tamaoka, A., Kondo, T., Odaka, A., Sahara, N., Sawamura, N., Ozawa, K., et al. (1994). Biochemical evidence for the long-tail form (A beta 1-42/43) of amyloid beta protein as a seed molecule in cerebral deposits of Alzheimer's disease. *Biochem. Biophys. Res. Commun.* 205, 834–842. doi: 10.1006/bbrc.1994.2740
- Teunissen, C. E., Verberk, I. M. W., Thijssen, E. H., Vermunt, L., Hansson, O., Zetterberg, H., et al. (2022). Blood-based biomarkers for Alzheimer's disease: towards clinical implementation. *Lancet Neurol.* 21, 66–77. doi: 10.1016/S1474-4422(21)00361-6
- Tolar, M., Abushakra, S., and Sabbagh, M. (2019). The path forward in Alzheimer's disease therapeutics: reevaluating the amyloid cascade hypothesis. *Alzheimers Dement.* 16, 1553–1560. doi: 10.1016/j.jalz.2019.09.075
- Trautenberg, H. L., Sommer, J.-U., and Goritz, D. (1995). Structure and swelling of end-linked model networks. *J. Chem. Soc. Faraday Trans.* 91, 2649–2653. doi: 10.1039/FT9959102649
- van der Schoot, P. (2005). "Theory of supramolecular polymerization," in *Supramolecular Polymers, 2nd Edn*, eds A. Ciferri (Boca Raton: CRC Press), 77–106.
- Wälti, M. A., Orts, J., Vögeli, B., Campioni, S., and Riek, R. (2015). Solution NMR studies of recombinant A β (1-42): from the presence of a micellar entity to residual β -sheet structure in the soluble species. *ChemBioChem* 16, 659–669. doi: 10.1002/cbic.201402595
- Weber, H., Paul, W., and Binder, K. (1999). Monte carlo simulation of a lyotropic first-order isotropic-nematic phase transition in a lattice polymer model. *Phys. Rev. E* 59, 2168–2174. doi: 10.1103/PhysRevE.59.2168
- Wegmann, S., Eftekharzadeh, B., Tepper, K., Zoltowska, K. M., Bennett, R. E., Dujardin, S., et al. (2018). Tau protein liquid-liquid phase separation can initiate tau aggregation. *EMBO J.* 37, e98049. doi: 10.15252/embj.201798049
- Wuttke, R., Hofmann, H., Nettels, D., Borgia, M. B., Mittal, J., Best, R. B., et al. (2014). Temperature-dependent solvation modulates the dimensions of disordered proteins. *Proc. Natl. Acad. Sci. U.S.A.* 11, 5213–5218. doi: 10.1073/pnas.1313006111
- Yaffe, K., Weston, A., Graff-Radford, N. R., Satterfield, S., Simonsick, E. M., Younkin, S. G., et al. (2011). Association of plasma beta-amyloid level and cognitive reserve with subsequent cognitive decline. *JAMA* 305, 261–266. doi: 10.1001/jama.2010.1995
- Yan, Y., and Wang, C. (2007). A β 40 protects non-toxic A β 42 monomer from aggregation. *J. Mol. Biol.* 369, 909–916. doi: 10.1016/j.jmb.2007.04.014
- Zetterberg, H. (2019). Blood-based biomarkers for Alzheimer's disease—an update. *J. Neurosci. Methods* 319, 2–6. doi: 10.1016/j.jneumeth.2018.10.025
- Zhang, Q., Sidorenko, J., Couvy-Duchesne, B., Marioni, R. E., Wright, M. J., Goate, A. M., et al. (2020). Risk prediction of late-onset Alzheimer's disease implies an oligogenic architecture. *Nat. Commun.* 11, 4799. doi: 10.1038/s41467-020-18534-1
- Zhang, Y.-W., Thompson, R., Zhang, H., and Xu, H. (2011). APP processing in Alzheimer's disease. *Mol. Brain* 4, 3. doi: 10.1186/1756-6606-4-3
- Zhao, N., Ren, Y., Yamazaki, Y., Qiao, W., Li, F., Felton, L. M., et al. (2020). Alzheimer's risk factors age, APOE genotype, and sex drive distinct molecular pathways. *Neuron* 106, 727.e6–742.e6. doi: 10.1016/j.neuron.2020.02.034
- Zhu, X., Bora, R. P., Barman, A., Singh, R., and Prabhakar, R. (2012). Dimerization of the full-length Alzheimer amyloid β -peptide (A β 42) in explicit aqueous solution: a molecular dynamics study. *J. Phys. Chem. B* 116, 4405–4416. doi: 10.1021/jp210019h